

Holographic study of higher-order baryon number susceptibilities at finite temperature and density

Zhibin Li^{1,‡}, Jingmin Liang^{1,§}, Song He^{2,3,*} and Li Li^{4,5,6,†}

¹*School of Physics and Microelectronics, Zhengzhou University, Zhengzhou 450001, China*

²*Center for Theoretical Physics and College of Physics, Jilin University, Changchun 130012, China*

³*Max Planck Institute for Gravitational Physics (Albert Einstein Institute),
Am Mühlenberg 1, 14476 Golm, Germany*

⁴*CAS Key Laboratory of Theoretical Physics, Institute of Theoretical Physics,
Chinese Academy of Sciences, Beijing 100190, China*

⁵*School of Fundamental Physics and Mathematical Sciences, Hangzhou Institute for Advanced Study,
University of Chinese Academy of Sciences, Hangzhou 310024, China*

⁶*Peng Huanwu Collaborative Center for Research and Education, Beihang University,
Beijing 100191, China*



(Received 5 June 2023; accepted 26 July 2023; published 15 August 2023)

The cumulants of baryon number fluctuations serve as a good probe for experimentally exploring the QCD phase diagram at finite density, giving rise to characteristic fluctuation patterns associated with a possible critical endpoint (CEP). We compute the higher-order baryon number susceptibilities at finite temperature and baryon chemical potential using a holographic QCD model to address the nonperturbative aspect of strongly coupled QCD matter. The model can accurately confront lattice QCD data on a quantitative level and the location of the CEP is found to fall within the range accessible to upcoming experimental measurements. The baryon number susceptibilities up to the twelfth order are computed, and the collision energy dependence of different ratios of these susceptibilities is examined along the chemical freeze-out line. The holographic results show quantitative agreement with experimental data and the functional renormalization group results in a large collision energy range, with all ratios exhibiting a peak structure around 5–10 GeV. The mismatching between our holographic results with experimental data for sufficiently low-collision energy is possibly due to nonequilibrium effects and complex experimental environments. The future experiments with measurements in the low-collision energy range $\sqrt{s_{NN}} \approx 1$ –10 GeV and reduced experimental uncertainty could reveal more nonmonotonic behavior signals which can be used to locate the CEP.

DOI: [10.1103/PhysRevD.108.046008](https://doi.org/10.1103/PhysRevD.108.046008)

I. INTRODUCTION

Obtaining a quantitative understanding of the QCD phase diagram at finite temperature T and baryon chemical potential μ_B remains remarkably challenging due to the strongly coupled nature of the system under extreme conditions. Significant efforts have been devoted to this problem over the past few decades. Lattice QCD,

formulated on a grid of points in space and time, provides reliable information from first principles at small μ_B where the sign problem does not hinder numerical calculations. Lattice QCD calculations indicate that the chiral and confinement/deconfinement phase transitions likely occur as an analytic crossover for small μ_B , with mixing of the transitions [1–3]. On the other hand, several effective theories, including the Dyson-Schwinger equation (DSE) [4–9], the Nambu-Jona-Lasinio (NJL) model [10–13], and the functional renormalization group (FRG) [14–16], suggest the existence of a first-order phase transition at large μ_B , which would terminate at a critical point known as the QCD critical endpoint (CEP). However, the exact location of the CEP is still a matter of debate, with no conclusive constraints from any model calculations thus far. Nevertheless, lattice QCD results disfavor the existence of the CEP for $\mu_B/T \leq 3$ and $\mu_B < 300$ MeV [17–22].

*Corresponding author: hesong@jlu.edu.cn

†Corresponding author: liliphy@itp.ac.cn

‡lizhibin@zzu.edu.cn

§liangjingmin@gs.zzu.edu.cn

Published by the American Physical Society under the terms of the Creative Commons Attribution 4.0 International license. Further distribution of this work must maintain attribution to the author(s) and the published article's title, journal citation, and DOI. Funded by SCOAP³.

The critical physics associated with the CEP is expected to have a localized impact in its vicinity [23]. Numerous theoretical studies have revealed intriguing nontrivial patterns in the ratios of conserved charge distributions C_n around the CEP [12,16,24–30]. Nonmonotonic variations of conserved charge fluctuations with respect to the T and μ_B along the phase boundary could arise from critical physics in the vicinity of a CEP which can serve as signals for CEP [31]. Experimental measurement has suggested a significant overlap between the chemical freeze-out region and the crossover region for $\mu_B/T \leq 3$ [32], implying that the freeze-out line is likely to pass through the vicinity of the CEP, provided that the CEP is not far beyond $\mu_B/T \approx 3$. This indicates that C_n and their ratios along the chemical freeze-out line may take similar nonmonotonic behavior [12,16,26,28–30,33–35]. Remarkably, these ratios can be directly linked to measurable quantities in experiments, such as the mean, variance, skewness, and kurtosis, making it feasible to locate the CEP by measuring cumulants of conserved charge distributions in experimental studies.

Indeed, the potential existence of the CEP and the first-order phase transition has motivated dedicated experimental programs, particularly in relativistic heavy-ion collisions. In heavy ion collisions, the early nonequilibrium state of quarks and gluons will become the final hadronic states after a chemical freeze-out. Moreover, regions of large μ_B can be experimentally researched by lowering the beam energy. In recent years, relativistic heavy-ion collision experiments have made significant progress in the search for the CEP [36,37]. Various cumulants, including net-proton, net-charge, and net-kaon cumulants, have been measured at different collision energies. Notably, recent STAR data on net-proton distributions $\kappa\sigma^2$ in Au + Au collisions as a function of collision energy $\sqrt{s_{NN}}$ shows a nonmonotonic variation, exhibiting a peak structure near $\sqrt{s_{NN}} \approx 7$ GeV, which could be an experimental signature of the CEP [38–41]. Furthermore, measurements have been extended to higher-order cumulants, including the sixth-order [42] and eighth-order [43] cumulants of net-proton fluctuations. Nonmonotonic dependencies on collision energy have also been observed in the fifth-order and sixth-order cumulant data of net-proton fluctuations in 0–40% centrality Au-Au collisions [42].

Given the limited experimental data available that is confined to the crossover region with $\mu_B/T \leq 3$, it is crucial to deepen our understanding of conserved charge fluctuations at high μ_B , where lattice simulations face challenges due to the sign problem. To address this nonperturbative aspect, we employ holographic duality to map the strongly correlated physics of the QCD phase diagram to a higher-dimensional gravity system. Holography offers a convenient framework to incorporate real-time dynamics and study transport properties at finite temperatures and densities. Our holographic model has been demonstrated to

capture the essential characteristics of realistic QCD and successfully confront lattice QCD data with 2 + 1 flavors on a quantitative level [44]. We have constructed the phase diagram in terms of T and μ_B , and determined the location of the CEP at $(T_{CEP} = 105 \text{ MeV}, \mu_{CEP} = 555 \text{ MeV})$ which falls within the range accessible to upcoming experimental measurements [44]. In this study, we shall investigate the behavior of baryon number fluctuations over a wide range of temperatures and baryon chemical potentials. We will compare our holographic results with the experimental measurements and will provide further theoretical predictions.¹

The rest of this paper is organized as follows. In Sec. II, we briefly review our holographic QCD model, including optimized parameters and equations of states. Section III shows the baryon number susceptibilities up to the twelfth order at $\mu_B = 0$. We also compare our holographic results with the lattice QCD data. Section IV compares our results to available experimental data from heavy ion collisions along the chemical freeze-out line. We will present the prediction for the beam energy dependence of baryon number susceptibilities for which no experimental data is available yet. We conclude with some discussion in Sec. V.

II. HOLOGRAPHIC QCD MODEL

We consider the (2 + 1)-flavor holographic QCD model established in [44]. The gravitational action takes the following form.

$$S_M = \frac{1}{2\kappa_N^2} \int d^5x \sqrt{-g} \left[\mathcal{R} - \frac{1}{2} \nabla_\mu \phi \nabla^\mu \phi - \frac{Z(\phi)}{4} F_{\mu\nu} F^{\mu\nu} - V(\phi) \right], \quad (2.1)$$

with $g_{\mu\nu}$ the metric of the bulk spacetime, ϕ the scalar field, and A_μ the gauge field incorporating finite baryon chemical potential and baryon density. Here $V(\phi)$ and $Z(\phi)$ are two free couplings in our bottom-up model. The nonperturbative effects and flavor dynamics are effectively adopted into the model parameters by matching up-to-date lattice QCD data.²

The bulk spacetime metric with matter fields ϕ and A_μ reads

¹Previous studies on the baryon susceptibilities using holographic QCD can be found in [33,45,46]. The model was fixed by matching at zero baryon chemical potential to the lattice equation of state from [2]. It predicts a CEP at a significantly different location in the phase diagram from our model [44].

²This approach involving a bulk nonconformal dilatonic scalar and a $U(1)$ gauge field has been widely used in holographic QCD, see e.g., [29,46–60].

TABLE I. Parameters for our (2 + 1)-flavor QCD model by matching the lattice simulation.

Model	c_1	c_2	c_3	c_4	c_5	κ_N^2	ϕ_s [MeV]	b
2 + 1 flavor	0.710	0.0037	1.935	0.091	30	$2\pi(1.68)$	1085	-0.27341

$$ds^2 = -e^{-\eta(r)} f(r) dt^2 + \frac{dr^2}{f(r)} + r^2(dx_1^2 + dx_2^2 + dx_3^2),$$

$$\phi = \phi(r), \quad A_\mu dx^\mu = A_t(r) dt, \quad (2.2)$$

where r is the holographic radial coordinate for which $r \rightarrow \infty$ corresponds to the AdS boundary. Denoting the location of the event horizon as $r = r_h$ where $f(r_h) = 0$, the Hawking temperature and the entropy density are given by

$$T = \frac{1}{4\pi} f'(r_h) e^{-\eta(r_h)/2}, \quad s = \frac{2\pi}{\kappa_N^2} r_h^3. \quad (2.3)$$

Substituting (2.2) into the action (2.1), one obtains the equations of motion that have to be solved numerically to obtain the hairy black holes. Then, the related thermodynamic quantities, including the energy density \mathcal{E} , the pressure P , and the baryon chemical potential μ_B can be obtained using holographic renormalization (see [44] for more technical details).

The two couplings in (2.1) are parametrized to be [44]

$$V(\phi) = -12 \cosh[c_1 \phi] + \left(6c_1^2 - \frac{3}{2}\right) \phi^2 + c_2 \phi^6,$$

$$Z(\phi) = \frac{1}{1+c_3} \operatorname{sech}[c_4 \phi^3] + \frac{c_3}{1+c_3} e^{-c_5 \phi}, \quad (2.4)$$

where c_1 to c_5 are free parameters. The other two free parameters are the effective Newton constant κ_N^2 and a characteristic energy scale set by the leading source term of ϕ , i.e., $\phi_s = \lim_{r \rightarrow \infty} r\phi$. The latter breaks the scale invariance of the boundary system to essentially describe the

QCD dynamics as there is no conformal symmetry in real QCD. All the above parameters are fixed completely by fitting the lattice QCD data at zero net-baryon density [3,61,62] and their values are summarized in Table I.

The parameter b is from the holographic renormalization and is necessary to satisfy the lattice QCD simulation at $\mu_B = 0$. We have made a slight modification to the value of c_4 to enhance the agreement with lattice data compared to the previous setup [44]. Nevertheless, this modification yields almost the same location of the CEP as the one of [44]. We compare various thermodynamic quantities from our holographic setup with lattice simulation in Fig. 1. One case sees that the temperature dependence of all those quantities agrees well with lattice QCD with 2 + 1 flavors [3,61,62].

In addition, the dilaton potential $V(\phi)$ and gauge coupling $Z(\phi)$ employed in our present work yield a equation of state that exhibits good agreement with the state-of-the-art lattice QCD data at finite baryon chemical potential reported in [20] (see [44] for more details). Figure 2 illustrates the direct comparison of our $V(\phi)$ and $Z(\phi)$ with those utilized in other Einstein-Maxwell-Dilaton (EMD) models [46,54]. Notably, both functions, obtained by fitting distinct lattice QCD data, manifest significant universal characteristics. A recent review [63] also highlighted a similar comparison and proposed robust features of $V(\phi)$ and $Z(\phi)$ in the EMD description of lattice QCD results with 2 + 1 flavors and physical quark masses. Furthermore, the location of the CEP exhibits variations among these holographic EMD models, with $(T_{CEP}, \mu_{CEP}) = (105, 555)$ MeV [44], $(89, 724)$ MeV [46], and $(111.5, 611.5)$ MeV [54], respectively.

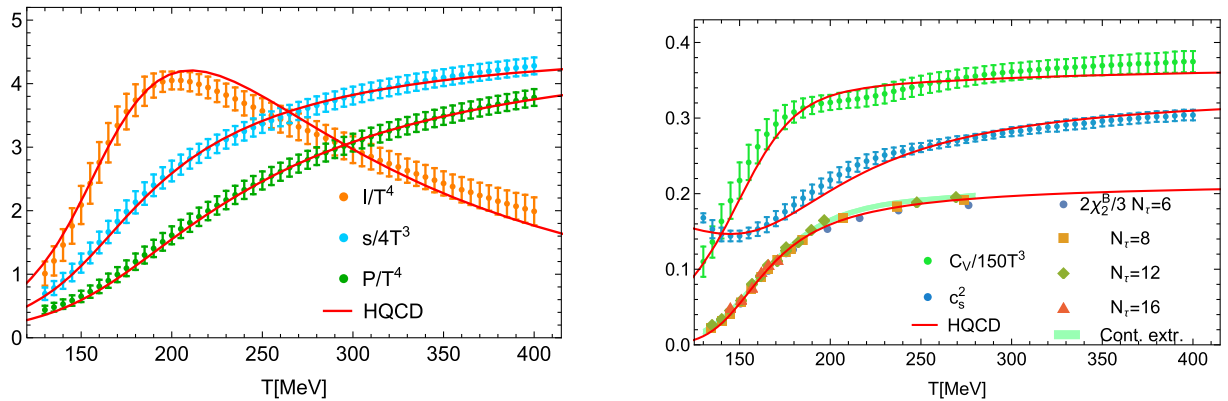


FIG. 1. Thermodynamics at $\mu_B = 0$ from lattice QCD results [3,61,62] compared to our holographic model (red solid curves). Left panel: the entropy density s , the pressure P , and the trace anomaly $I = \mathcal{E} - 3P$. Right panel: the specific heat C_V , the squared speed of sound c_s^2 , and the baryon susceptibility χ_B^2 .

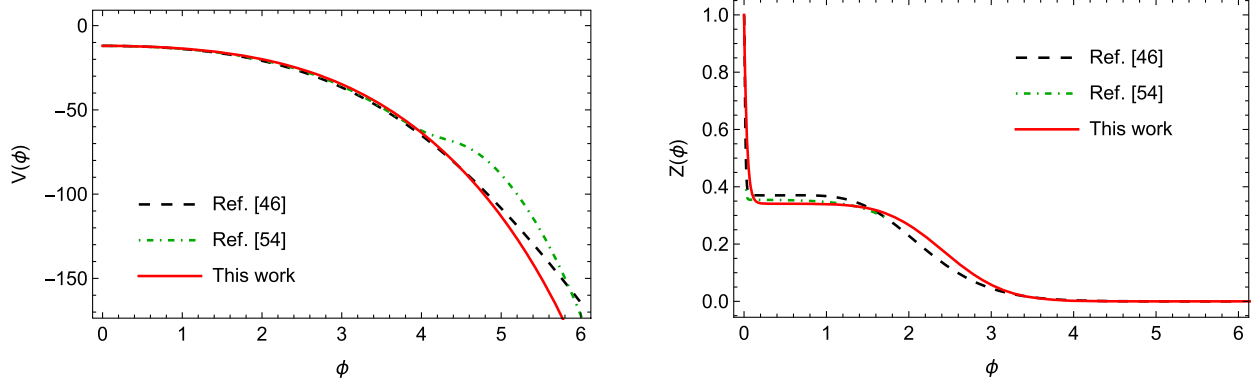


FIG. 2. Comparison between the dilaton potential $V(\phi)$ and gauge coupling $Z(\phi)$ used in our work [44] and those utilized in different holographic models [46,54]. Both functions obtained by fitting different lattice QCD data exhibit certain universal features. Furthermore, the CEP locations differ among various models, with the values of $(T_{CEP}, \mu_{CEP}) = (105, 555)$ MeV [44], $(89, 724)$ MeV [46], and $(111.5, 611.5)$ MeV [54], respectively.

The generalized susceptibilities are closely related to various cumulants of the baryon number distribution measured in heavy-ion collision experiments. Here we focus on the susceptibilities of the baryon number χ_n^B that are defined through the n th order derivatives of the pressure with respect to the baryon chemical potential.

$$\chi_n^B(T, \mu_B) = \frac{\partial^n}{\partial (\mu_B/T)^n} \frac{P}{T^4}. \quad (2.5)$$

For example, to apply the QCD simulation to a finite density case, one could consider a Taylor expansion in baryon chemical potential that underlies the extension of lattice results that are only available at $\mu_B = 0$.

$$\begin{aligned} & \frac{P(T, \mu_B) - P(T, 0)}{T^4} \\ &= \sum_{n=1}^{\text{inf}} \frac{\chi_{2n}^B(T)}{(2n)!} \left(\frac{\mu_B}{T}\right)^{2n} \\ &= \frac{1}{2} \chi_2^B(T) \hat{\mu}_B^2 \left(1 + \frac{1}{12} \frac{\chi_4^B(T)}{\chi_2^B(T)} \hat{\mu}_B^2 + \frac{1}{360} \frac{\chi_6^B(T)}{\chi_2^B(T)} \hat{\mu}_B^4 \right. \\ & \quad \left. + \frac{1}{20160} \frac{\chi_8^B(T)}{\chi_2^B(T)} \hat{\mu}_B^6 + \dots\right), \end{aligned} \quad (2.6)$$

where $\hat{\mu}_B = \mu_B/T$ is the reduced baryon chemical potential and $\chi_{2n}^B(T)$ are baryon number susceptibilities at $\mu_B = 0$. Note that $\chi_{2n+1}^B(T, \mu_B = 0) = 0$ due to the CP symmetry.

The corresponding cumulant of baryon distribution is given by

$$C_n^B = VT^3 \chi_n^B, \quad (2.7)$$

with V the freeze-out volume in heavy-ion collisions. The ratios of these cumulants cancel out volume dependence and are observable quantities in experiments. In particular,

the skewness S_B and the kurtosis κ_B of baryon distribution are given by

$$S_B = \frac{C_3^B}{(\sigma_2^B)^{3/2}} \quad \text{and} \quad \kappa_B = \frac{C_4^B}{(\sigma_2^B)^2}, \quad (2.8)$$

with the notation $M_B = C_1^B$ for the mean and $\sigma_2^B = C_2^B$ for the variance.

III. BARYON NUMBER SUSCEPTIBILITY AT $\mu_B = 0$

As a benchmark test, we present the numerical results of the baryon number susceptibilities at $\mu_B = 0$ and compare them with available lattice QCD simulation.

The behavior of χ_2^B has been depicted in the right panel of Fig. 1. One can see clearly that the holographic result is in good agreement with the latest lattice data from HotQCD group [62]. We compare higher-order susceptibilities in Fig. 3. The top two plots are for χ_4^B/χ_2^B and χ_6^B/χ_2^B , respectively. The points with error bars are the lattice data with different N_τ , and the light-blue band represents the region of continuous extrapolation based on the lattice data [19,62,64]. The holographic QCD results are given by solid red curves. Our direct computation matches well with the lattice data, particularly the results of the continuous extrapolation. The temperature dependence of χ_6^B and χ_8^B is presented in the bottom two plots of Fig. 3. Given that the uncertainty of the HotQCD data is relatively high. It is still challenging to analyze the behavior of χ_8^B . Nevertheless, our χ_8^B results qualitatively agree with those from the W-B data [65] and the FRG result [16].

While χ_2^B monotonically increases with the temperature at $\mu_B = 0$, higher-order susceptibilities versus temperature yield more complicated behaviors (see Fig. 3). The ratio χ_4^B/χ_2^B remains positive throughout but it initially increases to a peak at $T \approx 140$ MeV, before decreasing to

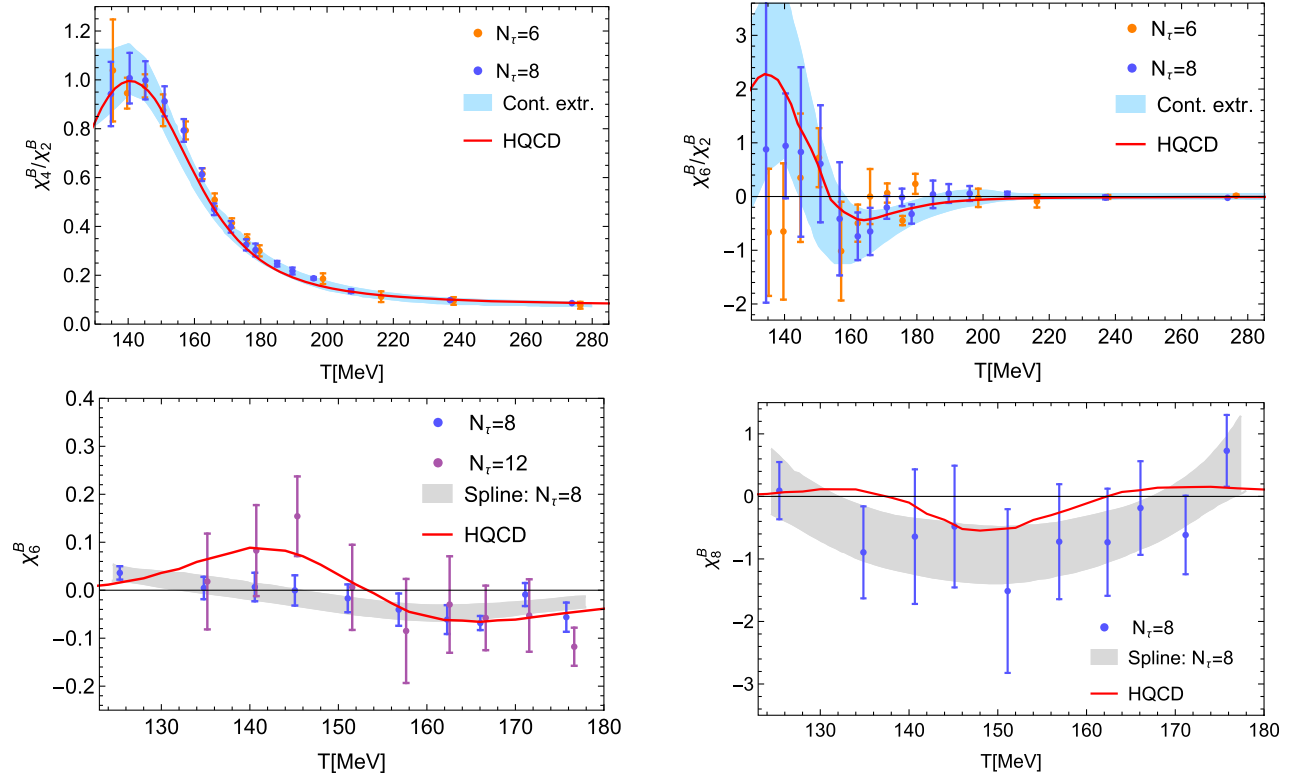


FIG. 3. Baryon number susceptibilities χ_4^B/χ_2^B (top left), χ_6^B/χ_2^B (top right), χ_6^B (bottom left), and χ_8^B (bottom right) at $\mu_B = 0$ compare with lattice data [19,62,64]. The light-blue band denotes the region of continuous extrapolation from lattice QCD simulation.

approximately 0.1 at high temperatures. Similarly, χ_6^B/χ_2^B exhibits an increase to about 2.2 at $T \approx 140$ MeV, followed by a decrease to -0.4 at $T \approx 165$ MeV and a subsequent increase to around 0. Thus, χ_6^B/χ_2^B displays a peak and a dip. The behavior of χ_6^B is similar to that of χ_6^B/χ_2^B due to the monotonically increasing dependence of χ_2^B on temperature. For χ_8^B , our holographic result suggests that it initially grows from 0 to approximately 0.2 by increasing T , then decreases to around -0.5 , and subsequently increases to 0.2 again at high temperatures.

There is no available lattice data for higher-order χ_n^B with $n \geq 10$ thus far. In Fig. 4, we show our theoretical computation for χ_{10}^B (left) and χ_{12}^B (right) as a function of temperature. Both cases display a more intricate behavior with temperature, featuring both increasing and decreasing trends, as well as positive and negative values. It will be of great interest to compare our results with future lattice QCD data for χ_{10}^B and χ_{12}^B , which would allow for a quantitative assessment of the accuracy of our model.

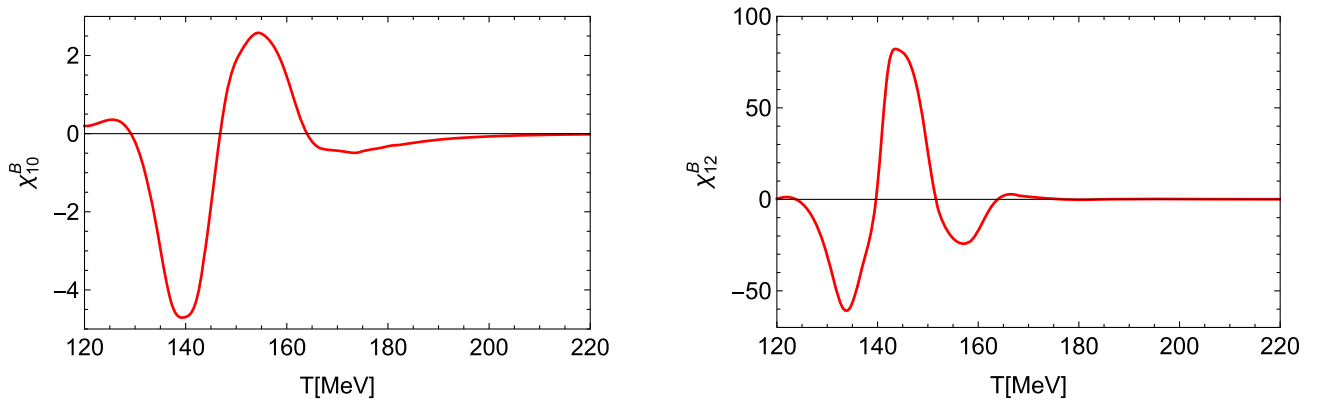


FIG. 4. The temperature dependence of higher order baryon number susceptibilities χ_{10}^B (left) and χ_{12}^B (right) from our holographic theory at $\mu_B = 0$.

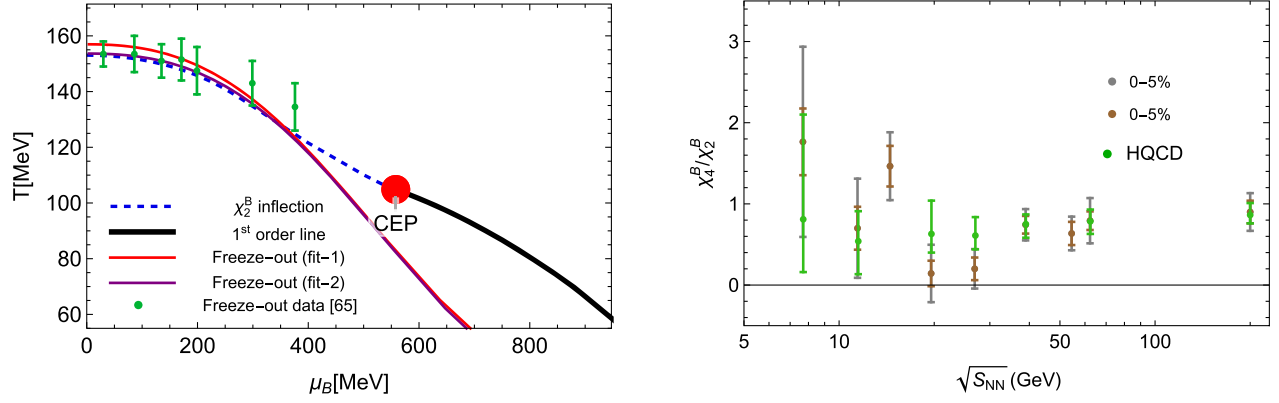


FIG. 5. Left panel: The phase diagram of our holographic QCD model, where the blue dashed line corresponds to the crossover line determined by χ_2^B inflection. The CEP is shown as a bold red dot. The thick black line represents the first-order transition line, while the red and purple lines depict the two fitted chemical freeze-out lines utilized in this study. The green data, accompanied by errors, corresponds to the chemical freeze-out data extracted from [66]. Right panel: χ_4^B/χ_2^B along the chemical freeze-out line compares with STAR data of net-proton distributions in 0–5% centrality Au–Au collisions [39]. The gray and brown error bars represent the statistical and systematic uncertainties, respectively. We have taken the position of chemical freeze-out directly from the HRG model [66].

IV. BARYON NUMBER SUSCEPTIBILITY ALONG CHEMICAL FREEZE-OUT LINES

In this section, we begin by examining the ratios of various higher-order baryon number susceptibilities at the collision energies measured by RHIC, following the chemical freeze-out data determined by Gupta *et al.* [66]. We will consider two fitted chemical freeze-out lines, aiming to capture the key characteristics of the CEP in the $T - \mu_B$ plane. As we will show, our theoretical predictions demonstrate some quantitative agreement with the most recent experimental data [38,39,42,43,67] as well as the results obtained from the FRG approach [16].

The phase diagram of our holographic QCD model is presented in the left panel of Fig. 5, wherein the blue dashed line corresponds to the crossover line determined by χ_2^B inflection. The location of CEP is marked by a bold red dot. The thick black line represents the first-order transition line,

while the red and purple lines depict the two chemical freeze-out lines fitted in our present work (see more details around Fig. 6 below). The green data, accompanied by errors, corresponds to the chemical freeze-out data given in the hadron resonance gas model [66]. In the right panel of Fig. 5, we present a comparison of the ratio of the fourth-order to second-order baryon number susceptibilities, χ_4^B/χ_2^B , obtained using our holographic QCD model for collision energies of $\sqrt{S_{NN}} = 7.7, 11.5, 19.6, 27, 39, 62.4,$ and 200 GeV, with experimental data of net-proton distributions for 0–5% centrality Au–Au collisions from STAR [39]. The gray and brown error bars represent the statistical and systematic uncertainties of the experimental data points, respectively. The fitted positions on the $T - \mu_B$ phase diagram for various collision energies have been obtained from [66]. It is worth noting that the uncertainty in our theoretical results is attributed to the imprecision in determining the location of the fixed collision energy on the

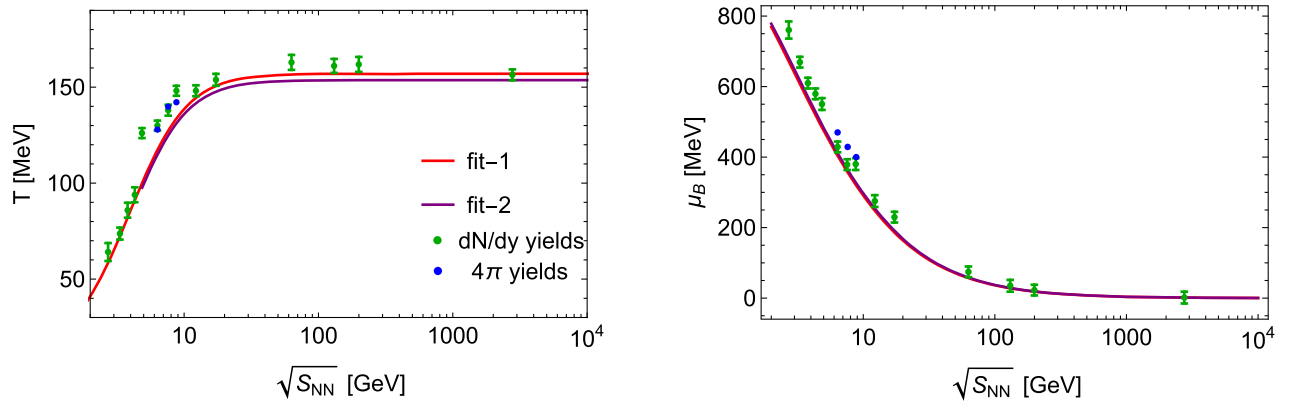


FIG. 6. The two chemical freeze-out lines we used in this work by fitting the dN/dy and 4π yields data [68,69]. The locations of the two fitted chemical freeze-out lines can be observed in the left panel of Fig. 5, within the context of the phase diagram. Left panel: The temperature as a function of the collision energy. Right panel: The baryon chemical potential versus the collision energy.

TABLE II. Parameters for two chemical freeze-out lines in Fig. 6 by matching the dN/dy and 4π yields data in [68,69].

	a [MeV]	b	T_{lim} [MeV]	c	d	e
Fit-1	1307.5	0.35	157.0	3.25	1	0.7
Fit-2	1307.5	0.34	153.6	3.41	1.1	0.6

$T - \mu_B$ phase diagram [66]. The direct comparison of Fig. 5, without any adjustable parameters, demonstrates a significant overlap between our theoretical results and experimental data at different collision energies.

Different centrality in heavy-ion collisions corresponds to different positions of chemical freeze-out in the $T - \mu_B$ phase diagram [32]. Therefore, one should choose an appropriate freeze-out line for a given centrality [70]. In

the present study, we consider two chemical freeze-out lines by fitting the dN/dy and 4π yields data in [68,69]. Also note that our fitting procedure does not yield a unique “optimal” fit for the data in [68,69], as we aim to optimize both the range of experimentally fitted freeze-out data and the degree of agreement between theoretical values of χ_m^B/χ_n^B and experimental data. Figure 6 displays the chemical freeze-out lines corresponding to centrality ranges of 0–5% (red line) and 0–40% (purple line), respectively. The fitting formula for the two chemical freeze-out lines is given by

$$\mu_B = \frac{a}{1 + b\sqrt{S_{NN}}},$$

$$T = \frac{T_{\text{lim}}}{1 + \exp[c - \ln(d\sqrt{S_{NN}} + e)/0.45]}, \quad (4.1)$$

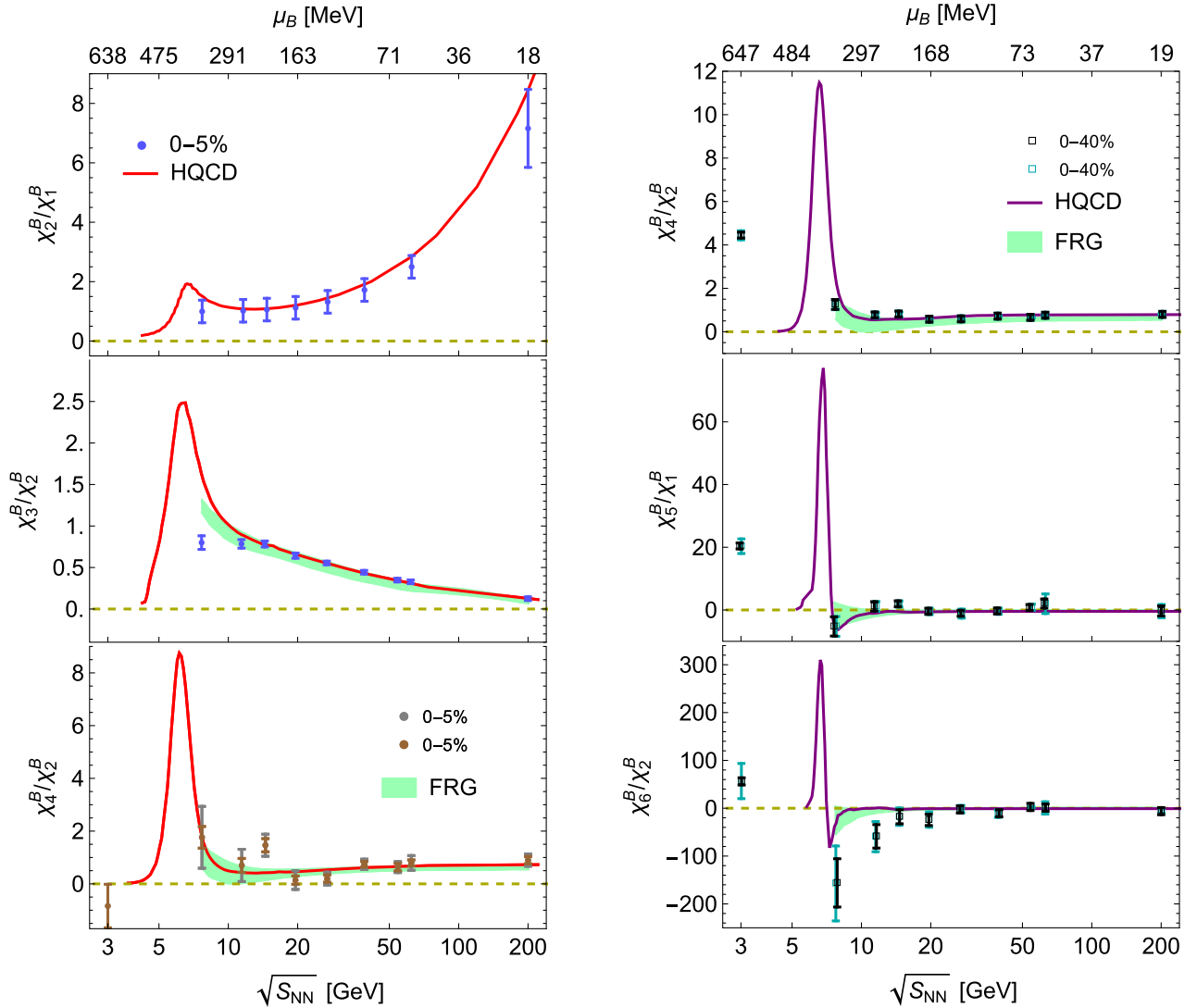


FIG. 7. Comparison between the baryon number susceptibilities along two fitted chemical freeze-out lines and the STAR data of net-proton distributions for centrality 0–5% (left) [38,39,67,71] and 0–40% (right) [42] Au-Au collisions, respectively. The error bars in the left panel (gray and brown) and the right panel (black and cyan) respectively denote the statistical and systematic uncertainties. The FRG results [16] are shown in green bands.

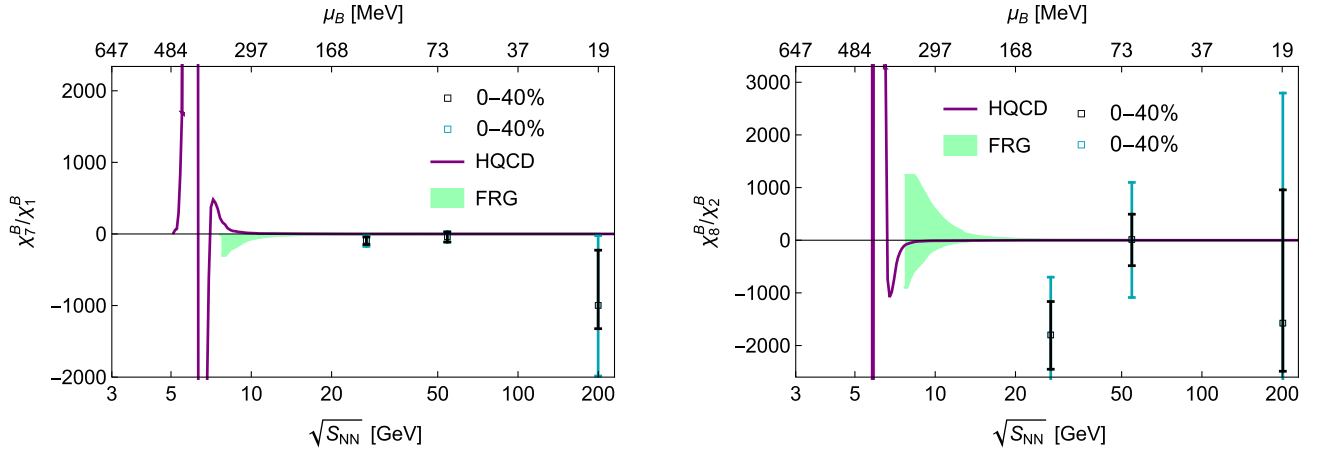


FIG. 8. Comparison between the baryon number susceptibilities χ_7^B/χ_1^B and χ_8^B/χ_2^B along fitted chemical freeze-out line “fit-2” and the STAR data of net-proton distributions in 0–40% [43] centrality Au-Au collisions. The black and cyan error bars correspond to the statistical and systematic uncertainties of the experimental data points, respectively. The FRG results [16] are denoted by green bands.

with $a, b, c, d, e, T_{\text{lim}}$ free parameters. The corresponding parameters used to fit both lines of Fig. 6 are summarized in Table II. The resulting freeze-out lines are shown in the $T - \mu_B$ phase diagram for both cases in the right panel of Fig. 5.

In Fig. 7, we present a direct comparison between the baryon number susceptibilities computed using our fitted chemical freeze-out lines and the experimental data from STAR with centrality ranges of 0–5% (left) [38,39,67] and 0–40% (right) [42]. The different error bars of Fig. 7, gray and brown in the left panel as well as black and cyan in the right panel, corresponding to the statistical and systematic uncertainties of the experimental data points, respectively. Moreover, we also include the FRG results denoted as green bands [16]. Our results demonstrate quantitative agreement with both STAR and FRG results for second and third-order baryon number susceptibilities in the collision energy range of $\sqrt{s_{NN}} \approx 12\text{--}200$ GeV. Interestingly, at lower-collision energies ($\sqrt{s_{NN}} \approx 5\text{--}10$ GeV), our results reveal a peak structure for both χ_2^B/χ_1^B and χ_3^B/χ_2^B , which is not reflected in the experimental data. From fourth to sixth order, our results show quantitative agreement with experimental data and FRG results in the collision energy range of $\sqrt{s_{NN}} \approx 7.7\text{--}200$ GeV for both centralities. Remarkably, the ratios χ_m^B/χ_n^B with $m > n$ in our model form a peak structure around $\sqrt{s_{NN}} \approx 5\text{--}10$ GeV, with the peak becoming sharper and larger as we progress to higher orders.

We also find that at collision energies below $\sqrt{s_{NN}} \approx 5$ GeV, the ratios χ_m^B/χ_n^B obtained from our model approach zero, which deviates from the STAR data of centrality 0–40% [42] (see the right column of Fig. 7). Such discrepancy observed at low-collision energies could stem from several factors, including nonequilibrium effects of low-energy collisions and complex experimental

environments (such as rotation and magnetic field³ in noncentric collisions). Therefore, further studies are necessary to investigate the role of these effects on the above-observed discrepancy.

Thus far, there are few experimental data for higher-order susceptibilities. Our prediction for χ_7^B/χ_1^B and χ_8^B/χ_2^B is presented in Fig. 8. The experimental data from STAR with the centrality of 0–40% [43] and the FRG results [16] are also included as a comparison. Current STAR data only includes points with collision energies of 27 GeV, 54.4 GeV, and 200 GeV, and the uncertainty is relatively high, making it challenging to identify nonmonotonic behavior from the data. Nevertheless, our results suggest that higher-order baryon number susceptibilities will exhibit more pronounced nonmonotonic behavior, with additional peaks and dips appearing along the freeze-out line. These features could be potentially observed in future experiments with improved precision.

V. CONCLUSION

In this study, we have investigated the behavior of higher-order baryon number susceptibilities (χ_n^B) at finite temperature and baryon chemical potential using a quantitative holographic QCD model that has been calibrated with lattice QCD data. We have observed a quantitative agreement between our results and the HotQCD lattice data at $\mu_B = 0$, see Figs. 1 and 3. The examination of χ_{10}^B and χ_{12}^B will be possible in the future once relevant lattice data becomes available.

To investigate the critical physics associated with the CEP, we have analyzed the dependence of various ratios of χ_n^B on collision energy along the chemical freeze-out line. Our

³The rotation and magnetic field effects in holographic QCD was investigated e.g., in [72–77].

findings demonstrate a quantitative agreement with experimental data from STAR net-proton high moments in 0–5% centrality and 0–40% centrality Au-Au collisions, as well as FRG results for second and third-order baryon number susceptibilities within the range $\sqrt{S_{NN}} \approx 12\text{--}200$ GeV. At lower collision energies, we have observed a clear peak structure from χ_2^B/χ_1^B and χ_3^B/χ_2^B around $\sqrt{S_{NN}} \approx 5\text{--}10$ GeV (see Fig. 7), while experimental data is accumulating to check this feature. Regarding the fourth- to sixth-order ratios, our results have exhibited quantitative agreement with experimental data and FRG results over a broad collision energy range of $\sqrt{S_{NN}} \approx 7.7\text{--}200$ GeV. We have found that all ratios χ_m^B/χ_n^B with $m > n$ display peak structures around $\sqrt{S_{NN}} \approx 5\text{--}10$ GeV, characterized by sharper and higher peaks as m is increased.

However, for low collision energies ($\sqrt{S_{NN}} < 5$ GeV), the ratios χ_m^B/χ_n^B tend to approach zero, which deviates from the STAR data. This discrepancy can potentially be attributed to nonequilibrium effects present in low-energy collisions, as well as the influence of complex experimental environments, such as rotation and magnetic field effects in noncentral collisions. Notably, it has been proposed that

rotation might have a significant impact on the results obtained from low-energy collisions. Therefore, we suggest that future experiments with measurements conducted in the low-collision energy range of $\sqrt{S_{NN}} \approx 1\text{--}10$ GeV, along with reduced experimental uncertainties, will unveil further nonmonotonic behavioral signals that could aid in the precise determination of the location of the CEP.

ACKNOWLEDGMENTS

We would like to thank Yong Cai, Wei-Jie Fu, De-Fu Hou, Cheng-Ming Li, Shu Lin, Peng Liu, Xiaofeng Luo, Shi Pu, and Yi-Bo Yang for their helpful discussion. S. H. would appreciate the financial support from the Fundamental Research Funds for the Central Universities and Max Planck Partner Group, as well as the Natural Science Foundation of China (NSFC) Grants No. 12075101 and No. 12235016. L. L. was partially supported by the NSFC Grants No. 12122513, No. 12075298, and No. 12047503, and by the Chinese Academy of Sciences Project for Young Scientists in Basic Research YSBR-006.

-
- [1] S. Borsanyi, G. Endrodi, Z. Fodor, A. Jakovac, S. D. Katz, S. Krieg, C. Ratti, and K. K. Szabo, The QCD equation of state with dynamical quarks, *J. High Energy Phys.* **11** (2010) 077.
 - [2] S. Borsanyi, Z. Fodor, C. Hoelbling, S. D. Katz, S. Krieg, and K. K. Szabo, Full result for the QCD equation of state with 2 + 1 flavors, *Phys. Lett. B* **730**, 99 (2014).
 - [3] A. Bazavov *et al.* (HotQCD Collaboration), Equation of state in (2 + 1)-flavor QCD, *Phys. Rev. D* **90**, 094503 (2014).
 - [4] X.-y. Xin, S.-x. Qin, and Y.-x. Liu, Quark number fluctuations at finite temperature and finite chemical potential via the Dyson-Schwinger equation approach, *Phys. Rev. D* **90**, 076006 (2014).
 - [5] F. Gao and Y.-x. Liu, QCD phase transitions via a refined truncation of Dyson-Schwinger equations, *Phys. Rev. D* **94**, 076009 (2016).
 - [6] S.-x. Qin, L. Chang, H. Chen, Y.-x. Liu, and C. D. Roberts, Phase Diagram and Critical Endpoint for Strongly-Interacting Quarks, *Phys. Rev. Lett.* **106**, 172301 (2011).
 - [7] C. Shi, Y.-L. Wang, Y. Jiang, Z.-F. Cui, and H.-S. Zong, Locate QCD critical end point in a continuum model study, *J. High Energy Phys.* **07** (2014) 014.
 - [8] C. S. Fischer, J. Luecker, and C. A. Welzbacher, Phase structure of three and four flavor QCD, *Phys. Rev. D* **90**, 034022 (2014).
 - [9] F. Gao and J. M. Pawłowski, QCD phase structure from functional methods, *Phys. Rev. D* **102**, 034027 (2020).
 - [10] M. Asakawa and K. Yazaki, Chiral restoration at finite density and temperature, *Nucl. Phys.* **A504**, 668 (1989).
 - [11] T. M. Schwarz, S. P. Klevansky, and G. Papp, The phase diagram and bulk thermodynamical quantities in the NJL model at finite temperature and density, *Phys. Rev. C* **60**, 055205 (1999).
 - [12] Z. Li, K. Xu, X. Wang, and M. Huang, The kurtosis of net baryon number fluctuations from a realistic Polyakov–Nambu–Jona-Lasinio model along the experimental freeze-out line, *Eur. Phys. J. C* **79**, 245 (2019).
 - [13] P. Zhuang, M. Huang, and Z. Yang, Density effect on hadronization of a quark plasma, *Phys. Rev. C* **62**, 054901 (2000).
 - [14] W.-j. Fu, J. M. Pawłowski, and F. Rennecke, QCD phase structure at finite temperature and density, *Phys. Rev. D* **101**, 054032 (2020).
 - [15] H. Zhang, D. Hou, T. Kojo, and B. Qin, Functional renormalization group study of the quark-meson model with ω meson, *Phys. Rev. D* **96**, 114029 (2017).
 - [16] W.-j. Fu, X. Luo, J. M. Pawłowski, F. Rennecke, R. Wen, and S. Yin, Hyper-order baryon number fluctuations at finite temperature and density, *Phys. Rev. D* **104**, 094047 (2021).
 - [17] V. Vovchenko, J. Steinheimer, O. Philipsen, and H. Stoecker, Cluster expansion model for QCD baryon number fluctuations: No phase transition at $\mu_B/T < \pi$, *Phys. Rev. D* **97**, 114030 (2018).
 - [18] S. Borsanyi, Z. Fodor, J. N. Guenther, R. Kara, S. D. Katz, P. Parotto, A. Pasztor, C. Ratti, and K. K. Szabo, QCD

- Crossover at Finite Chemical Potential from Lattice Simulations, *Phys. Rev. Lett.* **125**, 052001 (2020).
- [19] A. Bazavov *et al.*, Skewness, kurtosis, and the fifth and sixth order cumulants of net baryon-number distributions from lattice QCD confront high-statistics STAR data, *Phys. Rev. D* **101**, 074502 (2020).
- [20] S. Borsányi, Z. Fodor, J. N. Guenther, R. Kara, S. D. Katz, P. Parotto, A. Pásztor, C. Ratti, and K. K. Szabó, Lattice QCD Equation of State at Finite Chemical Potential from an Alternative Expansion Scheme, *Phys. Rev. Lett.* **126**, 232001 (2021).
- [21] D. Bollweg, D. A. Clarke, J. Goswami, O. Kaczmarek, F. Karsch, S. Mukherjee, P. Petreczky, C. Schmidt, and S. Sharma, Equation of state and speed of sound of $(2+1)$ -flavor QCD in strangeness-neutral matter at non-vanishing net baryon-number density, *Phys. Rev. D* **108**, 014510 (2023).
- [22] O. Philipsen, Lattice constraints on the QCD chiral phase transition at finite temperature and baryon density, *Symmetry* **13**, 2079 (2021).
- [23] B.-J. Schaefer and J. Wambach, Susceptibilities near the QCD (tri)critical point, *Phys. Rev. D* **75**, 085015 (2007).
- [24] M. Asakawa, S. Ejiri, and M. Kitazawa, Third Moments of Conserved Charges as Probes of QCD Phase Structure, *Phys. Rev. Lett.* **103**, 262301 (2009).
- [25] B. J. Schaefer and M. Wagner, QCD critical region and higher moments for three flavor models, *Phys. Rev. D* **85**, 034027 (2012).
- [26] W. Fan, X. Luo, and H.-S. Zong, Mapping the QCD phase diagram with susceptibilities of conserved charges within Nambu–Jona-Lasinio model, *Int. J. Mod. Phys. A* **32**, 1750061 (2017).
- [27] I. Portillo, Susceptibilities from a black hole engineered EoS with a critical point, *J. Phys. Conf. Ser.* **832**, 012041 (2017).
- [28] W. Fan, X. Luo, and H. Zong, Probing the QCD phase structure with higher order baryon number susceptibilities within the NJL model, *Chin. Phys. C* **43**, 033103 (2019).
- [29] Z. Li, Y. Chen, D. Li, and M. Huang, Locating the QCD critical end point through the peaked baryon number susceptibilities along the freeze-out line, *Chin. Phys. C* **42**, 013103 (2018).
- [30] Y.-P. Zhao, C.-Y. Wang, S.-Y. Zuo, and C.-M. Li, Non-extensive effects on QCD chiral phase diagram and baryon-number fluctuations within Polyakov-Nambu–Jona-Lasinio model, *Chin. Phys. C* **47**, 053103 (2023).
- [31] M. A. Stephanov, On the Sign of Kurtosis Near the QCD Critical Point, *Phys. Rev. Lett.* **107**, 052301 (2011).
- [32] L. Adamczyk *et al.* (STAR Collaboration), Bulk properties of the medium produced in relativistic heavy-ion collisions from the beam energy scan program, *Phys. Rev. C* **96**, 044904 (2017).
- [33] I. Portillo, Baryon susceptibilities from a holographic equation of state, *Nucl. Phys.* **A967**, 916 (2017).
- [34] X. Wang, M. Wei, Z. Li, and M. Huang, Quark matter under rotation in the NJL model with vector interaction, *Phys. Rev. D* **99**, 016018 (2019).
- [35] M. Huang and P. Zhuang, QCD matter and phase transitions under extreme conditions, *Symmetry* **15**, 541 (2023).
- [36] X. Luo and N. Xu, Search for the QCD critical point with fluctuations of conserved quantities in relativistic heavy-ion collisions at RHIC: An overview, *Nucl. Sci. Tech.* **28**, 112 (2017).
- [37] M. Abdallah *et al.* (STAR Collaboration), Cumulants and correlation functions of net-proton, proton, and antiproton multiplicity distributions in Au + Au collisions at energies available at the BNL Relativistic Heavy Ion Collider, *Phys. Rev. C* **104**, 024902 (2021).
- [38] J. Adam *et al.* (STAR Collaboration), Nonmonotonic Energy Dependence of Net-Proton Number Fluctuations, *Phys. Rev. Lett.* **126**, 092301 (2021).
- [39] M. S. Abdallah *et al.* (STAR Collaboration), Measurements of Proton High Order Cumulants in $\sqrt{s_{NN}} = 3$ GeV Au + Au Collisions and Implications for the QCD Critical Point, *Phys. Rev. Lett.* **128**, 202303 (2022).
- [40] A. Pandav, D. Mallick, and B. Mohanty, Search for the QCD critical point in high energy nuclear collisions, *Prog. Part. Nucl. Phys.* **125**, 103960 (2022).
- [41] Y. Zhang (STAR Collaboration), Higher-order proton cumulants in Au + Au collisions at $\sqrt{s_{NN}} = 3$ GeV from RHIC-STAR, *Acta Phys. Pol. B Proc. Suppl.* **16**, 45 (2023).
- [42] B. Aboona *et al.* (STAR Collaboration), Beam Energy Dependence of Fifth and Sixth-Order Net-proton Number Fluctuations in Au + Au Collisions at RHIC, *Phys. Rev. Lett.* **130**, 082301 (2023).
- [43] A. Pandav (STAR Collaboration), Seventh and eighth-order cumulants of net-proton multiplicity distributions in heavy-ion collisions at RHIC-STAR, *EPJ Web Conf.* **276**, 01006 (2023).
- [44] R.-G. Cai, S. He, L. Li, and Y.-X. Wang, Probing QCD critical point and induced gravitational wave by black hole physics, *Phys. Rev. D* **106**, L121902 (2022).
- [45] R. Rougemont, J. Noronha, and J. Noronha-Hostler, Suppression of Baryon Diffusion and Transport in a Baryon Rich Strongly Coupled Quark-Gluon Plasma, *Phys. Rev. Lett.* **115**, 202301 (2015).
- [46] R. Critelli, J. Noronha, J. Noronha-Hostler, I. Portillo, C. Ratti, and R. Rougemont, Critical point in the phase diagram of primordial quark-gluon matter from black hole physics, *Phys. Rev. D* **96**, 096026 (2017).
- [47] O. DeWolfe, S. S. Gubser, and C. Rosen, A holographic critical point, *Phys. Rev. D* **83**, 086005 (2011).
- [48] O. DeWolfe, S. S. Gubser, and C. Rosen, Dynamic critical phenomena at a holographic critical point, *Phys. Rev. D* **84**, 126014 (2011).
- [49] R.-G. Cai, S. He, and D. Li, A hQCD model and its phase diagram in Einstein-Maxwell-Dilaton system, *J. High Energy Phys.* **03** (2012) 033.
- [50] R.-G. Cai, S. Chakraborty, S. He, and L. Li, Some aspects of QGP phase in a hQCD model, *J. High Energy Phys.* **02** (2013) 068.
- [51] S. I. Finazzo and J. Noronha, Holographic calculation of the electric conductivity of the strongly coupled quark-gluon plasma near the deconfinement transition, *Phys. Rev. D* **89**, 106008 (2014).
- [52] Y. Yang and P.-H. Yuan, A refined holographic QCD model and QCD phase structure, *J. High Energy Phys.* **11** (2014) 149.
- [53] Y. Chen, M. Huang, and Q.-S. Yan, Gravitation waves from QCD and electroweak phase transitions, *J. High Energy Phys.* **05** (2018) 178.

- [54] J. Knaute, R. Yaresko, and B. Kämpfer, Holographic QCD phase diagram with critical point from Einstein–Maxwell-dilaton dynamics, *Phys. Lett. B* **778**, 419 (2018).
- [55] Z. Fang, Y.-L. Wu, and L. Zhang, Chiral phase transition and QCD phase diagram from AdS/QCD, *Phys. Rev. D* **99**, 034028 (2019).
- [56] A. Ballon-Bayona, H. Boschi-Filho, E. F. Capossoli, and D. M. Rodrigues, Criticality from Einstein-Maxwell-dilaton holography at finite temperature and density, *Phys. Rev. D* **102**, 126003 (2020).
- [57] M.-W. Li, Y. Yang, and P.-H. Yuan, Analytic study on chiral phase transition in holographic QCD, *J. High Energy Phys.* **02** (2021) 055.
- [58] J. Grefa, J. Noronha, J. Noronha-Hostler, I. Portillo, C. Ratti, and R. Rougemont, Hot and dense quark-gluon plasma thermodynamics from holographic black holes, *Phys. Rev. D* **104**, 034002 (2021).
- [59] S. He, L. Li, Z. Li, and S.-J. Wang, Gravitational waves and primordial black hole productions from gluodynamics, [arXiv:2210.14094](https://arxiv.org/abs/2210.14094).
- [60] J. Grefa, M. Hippert, J. Noronha, J. Noronha-Hostler, I. Portillo, C. Ratti, and R. Rougemont, QCD equilibrium and dynamical properties from holographic black holes, *Rev. Mex. Fis. Suppl.* **3**, 040910 (2022).
- [61] A. Bazavov *et al.* (HotQCD Collaboration), Fluctuations and correlations of net baryon number, electric charge, and strangeness: A comparison of lattice QCD results with the hadron resonance gas model, *Phys. Rev. D* **86**, 034509 (2012).
- [62] A. Bazavov *et al.*, The QCD equation of state to $\mathcal{O}(\mu_B^6)$ from lattice QCD, *Phys. Rev. D* **95**, 054504 (2017).
- [63] R. Rougemont, J. Grefa, M. Hippert, J. Noronha, J. Noronha-Hostler, I. Portillo, and C. Ratti, Hot QCD phase diagram from holographic Einstein-Maxwell-dilaton models, [arXiv:2307.03885](https://arxiv.org/abs/2307.03885).
- [64] D. Bollweg, J. Goswami, O. Kaczmarek, F. Karsch, S. Mukherjee, P. Petreczky, C. Schmidt, and P. Scior (HotQCD Collaboration), Taylor expansions and Padé approximants for cumulants of conserved charge fluctuations at non-vanishing chemical potentials, *Phys. Rev. D* **105**, 074511 (2022).
- [65] S. Borsanyi, Z. Fodor, J. N. Guenther, S. K. Katz, K. K. Szabo, A. Pasztor, I. Portillo, and C. Ratti, Higher order fluctuations and correlations of conserved charges from lattice QCD, *J. High Energy Phys.* **10** (2018) 205.
- [66] S. Gupta, D. Mallick, D. K. Mishra, B. Mohanty, and N. Xu, Freeze-out and thermalization in relativistic heavy ion collisions, [arXiv:2004.04681](https://arxiv.org/abs/2004.04681).
- [67] J. Xu, Energy dependence of moments of net-proton, net-kaon, and net-charge multiplicity distributions at STAR, *J. Phys. Conf. Ser.* **736**, 012002 (2016).
- [68] A. Andronic, P. Braun-Munzinger, and J. Stachel, The horn, the hadron mass spectrum and the QCD phase diagram: The statistical model of hadron production in central nucleus-nucleus collisions, *Nucl. Phys.* **A834**, 237c (2010).
- [69] A. Andronic, P. Braun-Munzinger, K. Redlich, and J. Stachel, Decoding the phase structure of QCD via particle production at high energy, *Nature (London)* **561**, 321 (2018).
- [70] G. Mukherjee, D. Dutta, and D. K. Mishra, Conserved number fluctuations under global rotation in a hadron resonance gas model, [arXiv:2304.14658](https://arxiv.org/abs/2304.14658).
- [71] H. S. Ko, Higher-order moments of net-proton and the QCD phase structure, *EPJ Web Conf.* **276**, 01019 (2023).
- [72] R. Rougemont, R. Critelli, and J. Noronha, Holographic calculation of the QCD crossover temperature in a magnetic field, *Phys. Rev. D* **93**, 045013 (2016).
- [73] S. I. Finazzo, R. Critelli, R. Rougemont, and J. Noronha, Momentum transport in strongly coupled anisotropic plasmas in the presence of strong magnetic fields, *Phys. Rev. D* **94**, 054020 (2016); **96**, 019903(E) (2017).
- [74] R. Critelli, Equilibrium and non-equilibrium properties of the QGP in a magnetic field: A holographic approach, *J. Phys. Conf. Ser.* **832**, 012047 (2017).
- [75] X. Chen, L. Zhang, D. Li, D. Hou, and M. Huang, Gluodynamics and deconfinement phase transition under rotation from holography, *J. High Energy Phys.* **07** (2021) 132.
- [76] Z. Fang, Y.-Y. Li, and Y.-L. Wu, QCD phase diagram with a background magnetic field in an improved soft-wall AdS/QCD model, *Eur. Phys. J. C* **81**, 545 (2021).
- [77] Y.-Q. Zhao, S. He, D. Hou, L. Li, and Z. Li, Phase diagram of holographic thermal dense QCD matter with rotation, *J. High Energy Phys.* **04** (2023) 115.